

RESEARCH ARTICLE

# Analysis of the impact of key similarity criteria numbers of TBCC inlet during the mode transition

L. Chen<sup>1,2</sup>, Y. Zhang<sup>1,2</sup>, Y.X. Xu<sup>2</sup>, Z.Y. Wang<sup>2</sup>, H.J. Tan<sup>2</sup> and H.C. Xue<sup>2</sup>

<sup>1</sup>Laboratory of Aerodynamics in Multiple Flow Regimes, China Aerodynamics Research and Development Center, Mianyang 621000, P.R. China

<sup>2</sup>College of Energy and Power Engineering, Key Laboratory of Inlet and Exhaust System Technology, Ministry of Education, Nanjing University of Aeronautics and Astronautics, Nanjing 210016, P.R. China

**Corresponding authors:** Y. Zhang; Email: [y.zhang@nuaa.edu.cn](mailto:y.zhang@nuaa.edu.cn); H.J. Tan; Email: [thj@263.net](mailto:thj@263.net)

**Received:** 25 March 2024; **Revised:** 7 June 2024; **Accepted:** 27 June 2024

**Keywords:** over-under TBCC inlet; mode transition; similar criterion; dynamic mesh; scale effect

## Abstract

A simplified configuration was developed to facilitate the mode transition process within an over-under Turbine-Based Combined Cycle (TBCC) inlet. Leveraging dynamic mesh technology, an unsteady numerical simulation of the mode transition was conducted, emphasising the flow characteristics of the mode transition and the impact of key similarity criteria numbers. The findings indicate that at an incoming Mach number of 2.0, the mode transition is paired with a continuous alteration in the capture mass flow of the high-speed duct. This continual change instigates the inlet unstarting, with subsequent flow characteristics being contingent on the historical effect, exhibiting a degree of hysteresis characteristics. When the scale effect is considered, it is observed that a larger model scale results in higher Reynolds ( $Re$ ) and Strouhal ( $St$ ) numbers. This directly contributes to a notable delay in the unstart moment, a decrease in the unstart interval, and an enlargement of the hysteresis loop. An examination of control variables reveals that the  $Re$  number marginally influences mode transition characteristics, while the  $St$  number's effect constitutes approximately 90% of the scale effect. This conclusively demonstrates that the  $St$  number is the predominant similarity criterion number in the mode transition process.

## Nomenclature

$Re$	Reynolds number
$St$	Strouhal number
$\alpha$	rotation angle of the splitter, deg
$L$	total length of inlet, mm
$\beta$	compression angle of first-stage compression, deg
$H_{cap1}$	capture height of the scramjet inlet, mm
$H_{out1}$	exit height of the scramjet inlet, mm
$H_{cap2}$	capture height of the turbine inlet, mm
$H_{in}$	entrance height of the turbine inlet, mm
$H_c$	throat height of the turbine inlet, mm
$H_{out2}$	exit height of the turbine inlet, mm
$T^*$	total temperature, K
$P^*$	total pressure, Pa
$Ma$	incoming Mach number
$\omega$	splitter's rotation speed, deg/s
$\delta$	nominal thickness of the boundary layer, mm
$\delta^*$	displacement thickness of the boundary layer, mm
$\theta$	momentum thickness of the boundary layer, mm

$t_{uns}$	unstart time, s
$t_{res}$	restart time, s
$\Delta T_{uns}$	unstart interval, s
$\Delta T_{hys}$	relative hysteresis interval, s
$\rho$	incoming flow density, kg/m <sup>3</sup>
$v$	airflow velocity, m/s
$d$	characteristic length, mm
$\mu$	viscosity coefficient

## 1.0 Introduction

The hypersonic vehicle, which anticipated to be key strategic weapons in future warfare scenarios, is expected to operate within flight envelopes spanning Mach number range 0 to 6.0. However, a single form of propulsion system, such as turbine or ramjet, cannot meet the wide speed range requirements [1]. Turbine-Based Combined Cycle (TBCC) propulsion system, a combination of turbine and ramjet engines, could provide enough thrust in the full flight envelope [2, 3]. Significant advancements in TBCC technology have been achieved by a number of projects globally, including the US J58 [4] and X-43B [5], Japan's ATREX and HYPR program [6–8], the UK's SABRE [9], and Germany's Sanger program [10, 11].

The inlet, a crucial component of the TBCC system, plays a significant role in the overall performance of the propulsion system. It is responsible for capturing, decelerating and pressurising the incoming flow, providing high-quality airflow to the downstream propulsion systems in different modes to fulfil the aircraft's operational requirements. During the operation of the TBCC, the low-speed phase operates in turbine mode, while the high-speed phase functions in scramjet mode. The transition between these two modes, known as mode transition, primarily involves the capture of airflow in high/low-speed ducts, typically achieved through splitter plate adjustments. This transition and the associated complex unsteady phenomena directly affect the fluidity of the mode transition [12], making the mode transition process a key technology in the development of combined cycle propulsion systems [13, 14].

Albertson [15] conducted a study revealing that the interference arising from high/low-speed ducts does not significantly affect the performance during the mode transition in the over-under TBCC inlet with an incoming Mach number of 4.03. Sanders [16] advanced this research by designing a splitter for mode transition control using a variable geometry system for a Mach 7.0 over-under TBCC inlet. This design was further developed into both small-scale (IMX) [17] and large-scale (LIMX) [18–20] models for wind tunnel testing. It is important to note that scaling the models inevitably leads to variations in both the Reynolds ( $Re$ ) number and the Strouhal ( $St$ ) number. Nevertheless, subsequent testing has shown that these models maintain excellent aerodynamic characteristics and demonstrate effective mode transition capabilities across different scales. However, it is acknowledged that the inlet may experience mode transition in off-design states during actual flight due to variations in the incoming Mach number. Yu [21], Li [22] and Xiang [23] have observed unstart/restart phenomena in the high-speed duct during experimental or numerical studies on the mode transition process of the over-under TBCC inlet at off-design incoming Mach numbers, and this phenomenon has obvious hysteresis characteristics. The influence of scale on these complex unsteady aerodynamic phenomena remains an underexplored area of study. In aerodynamics experimental research, ensuring geometric similarity and equivalent values for similarity criteria between the model and actual flow fields is paramount [24]. However, attaining complete similarity presents significant challenges, as not all similarity criteria are equally pertinent to a given experiment. Therefore, it is of utmost importance to ascertain the primary similarity criterion for the TBCC inlet mode transition experiments to accurately replicate the aerodynamic data of the physical object in flight conditions.

This paper designs a typical over-under TBCC inlet, using dynamic mesh technology to conduct unsteady numerical research on the mode transition process. The mode transition characteristics under

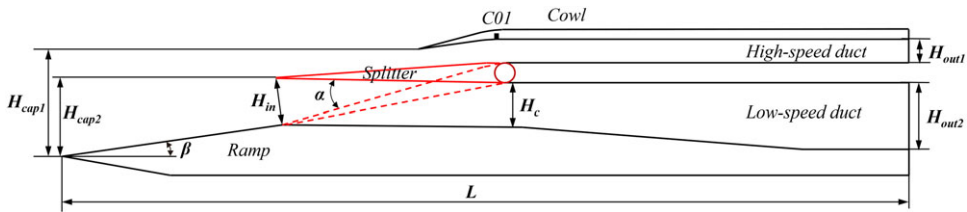


Figure 1. Schematic diagram of inlet.

off-design incoming Mach number conditions were investigated, and the scale effect analyses were conducted. Specifically, it examines the impact of critical similarity criteria— $Re$  and  $St$  numbers—on the mode transition behaviour. The paper aims to identify the dominant similarity criterion relationship of the scaling model and provide guiding data support for large-scale experiments.

## 2.0 Methodology

### 2.1 Description of the test model

The working Mach number for the over-under TBCC inlet, designed as this research, ranging from 0 to 6.0, with a transition Mach number specifically set at 3.0. As illustrated in Fig. 1, the inlet comprises two flow ducts: a high-speed scramjet duct and a low-speed turbine duct. The inlet's mode transition is facilitated by the splitter plate's rotational movement, depicted by the red line in the figure, which rotates at a total angle of  $11^\circ$ . The inlet's total length is  $L = 8,877$  mm, and its forebody is subjected to single-stage compression, which is shared evenly by the upper and lower ducts, and has a compression angle of  $\beta = 8^\circ$ . When operating solely on the scramjet duct, the splitter is entirely closed, as seen by the red dashed line in the figure. At this point, the scramjet inlet's capture height is  $H_{cap1} = 1,116$  mm, with the splitter doubling as a secondary compression surface at an angle of  $6.5^\circ$ . For the sake of research model simplification, the downstream channel is designed as a straight equal, with the channel's exit height set at  $H_{out1} = 245$  mm. Conversely, when the turbine duct is solely in operation, the splitter is fully opened, as shown by the red solid line in the figure. Under these conditions, the turbine inlet's capture height is  $H_{cap2} = 820$  mm, the duct's entrance height is  $H_{in} = 499$  mm, the throat height is  $H_c = 467$  mm, the exit height is  $H_{out2} = 700$  mm, and the internal contraction ratio (ICR) is  $ICR = H_{in}/H_c = 1.07$ . Lastly, it's essential to underline that this study intentionally omits the impact of downstream throttling and only focuses on the flow characteristics of the mode transition. Consequently, both the high-speed and low-speed ducts operate under unthrottled flow conditions.

### 2.2 Numerical approach

Two-dimensional dynamic mesh technology was implemented for grid division in this study. As depicted in Fig. 2, the main flow domain grid of the inlet employs structured grids, indicated by the yellow area in the figure. The rotational area of the splitter utilises triangular unstructured grids, represented by the green region in the figure. To capture the flow characteristics of the boundary layer near the splitter wall more effectively, structured grids marked by the blue area in the figure were employed adjacent to the splitter wall. Moreover, structured grids were utilised for near-wall surfaces throughout the entire domain, ensuring a  $y^+$  value of approximately 1 near the wall surface. Based on Ref. [25], the unsteady time step was set at  $5 \times 10^{-5}$  s, and the iterations of each sub-step was set to 300, resulting in a total grid size of roughly 300 thousand. It's important to note that the splitter couldn't be fully closed during calculations due to the structured mesh near the splitter and ramp walls. Thus, a unidirectional rotation stroke of the splitter was set at 10.5 degrees for the computations. The commercial CFD software

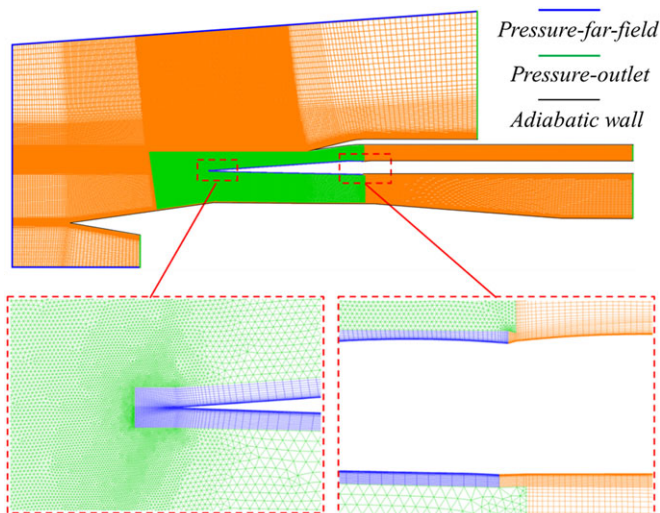


**Figure 2.** Computational meshes and boundary conditions.

ANSYS Fluent was employed for the numerical calculations. A finite volume method-based Navier–Stokes equation solver was used. Roe’s scheme was utilised for inviscid convection flux treatment, with the viscosity coefficient determined via the Sutherland formula. In turbulence modelling, the  $k$ - $\omega$  Shear Stress Transport (SST) model was adopted. Both the flow equation and turbulent transport equation were discretised using second-order accuracy schemes. The initial flowfield before the mode transition was obtained by steady numerical calculation using the same mesh.

In order to focus on the unstart and restart characteristics of the high-speed duct during mode transition, all conditions in this study were conducted under a Mach number of 2.0 which are below the design transition Mach number. As the numerical research performed in this study informs the subsequent small-scale wind tunnel test, the calculation conditions were aligned with the experimental conditions in FL-60, a 1.2 m  $\times$  1.2 m blowdown wind tunnel, located at Aerodynamics Research Institute, which is affiliated with Aviation Industry Corporation of China (AVIC). Specifically, the angle-of-attack was set at  $+4^\circ$ , the total temperature  $T^*$  was 300K, and the total pressure  $P^*$  was 194.8 kPa.

### 2.3 Numerical validation

The reliability of the steady numerical method was verified by selecting experimental results from Ref. [26]. The incoming Mach number was 4.92, the total temperature was 580K, and the static pressure was 0.7 MPa. Figure 3 illustrates a comparison between the numerical and experimental results. Figure 3(a) displays the numerical and experimental schlieren images, demonstrating a strong match in the boundary layer characteristics and shock system structure. Figure 3(b) compares the numerical and experimental data for the ramp and cowl wall pressure, utilising three varying grid numbers (coarse grid:  $1 \times 10^4$ , fine grid:  $1 \times 10^5$ , dense grid:  $1 \times 10^6$ ) to conduct grid sensitivity verification. The results show that all the grids align well with the experimental data, but the coarse grid shows minor inaccuracies in shoulder pressure measurement while the fine grid and dense grid show the same accuracy. Therefore, to balance prediction accuracy and time efficiency, subsequent calculations will employ the fine grid.

The experimental data derived from the rotating cowl with an incoming Mach number of 3.0 in Ref. [27], has been selected to validate the reliability of the unsteady calculations. Figure 4 presents the schematic diagram of the experimental model employed. During the experiment, the inlet was alternately unstarted and restarted by reciprocating the cowl. High-frequency pressure measurement points were established as shown in Fig. 5, which facilitated the acquisition of a hysteresis loop. The numerical

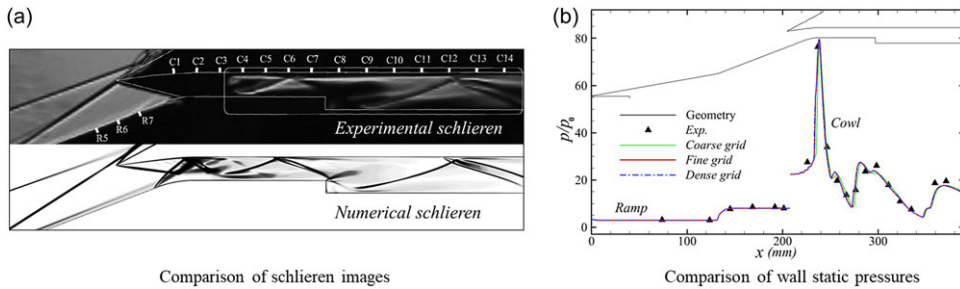


Figure 3. Comparisons of experimental and numerical results of inlet [26].

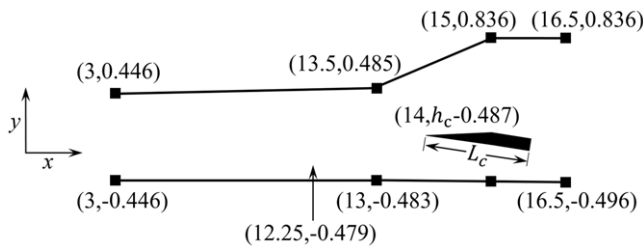


Figure 4. Schematic diagram of test model of Van Wie [27].

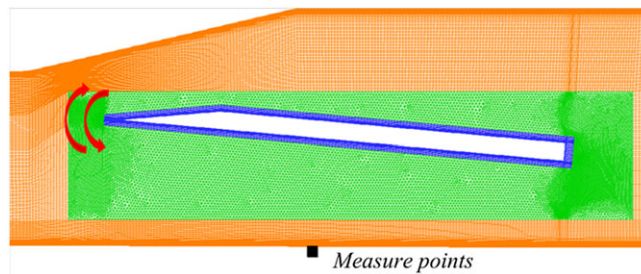
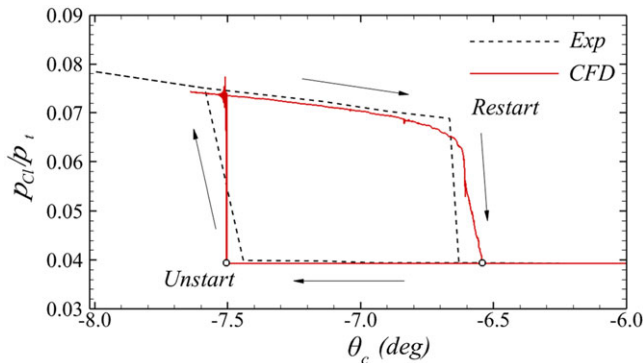


Figure 5. Schematic diagram of computational grid.

calculation of the experiment’s rotation process was conducted using dynamic mesh technology, which is same as the way in current paper. The schematic diagram of the mixed grid division was displayed in Fig. 5. The cowl rotation area, represented in green, utilised triangular unstructured grids, while structured grids were used elsewhere. The numerical hysteresis loop depicted in Fig. 6 correlates closely with the experimental outcomes of the unstart/restart process, validating that the unsteady numerical simulations, bolstered by the dynamic mesh technique, are reasonable.

### 3.0 Results and discussion

The flow characteristics of the over-under TBCC inlet mode transition under a representative off-design incoming Mach number were initially analysed. Subsequently, a scaling study was conducted to determine the impact of the scale effect on mode transition characteristics. Finally, by examining the control variables, the dominant similarity criterion in the mode transition process was identified, providing theoretical guidance and data support for large-scale experimental research.



**Figure 6.** Comparison of hysteresis loop in unstart/restart process.

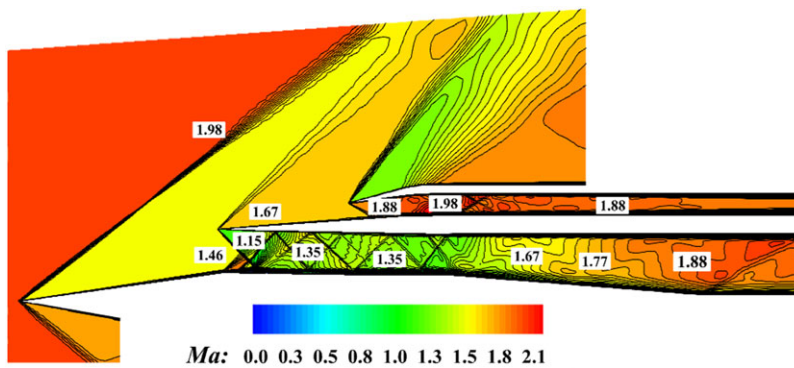


**Figure 7.** The initial flow field of  $M = 2.0$ .

### 3.1 Flow characteristics during mode transition

Figure 7 presents the Mach number contour map of the inlet prior to the inlet mode transition process at a Mach number of 2.0. It's evident that the airflow captured in the low-speed duct decelerates to a Mach number of 1.46 after passing through the shock induced by the first-stage compression ramp. Furthermore, it decelerates to a Mach number of 1.35 at the throat due to the simultaneous action of the shoulder expansion fan and cowl shock, before expanding in the expansion channel downstream of the throat. Meanwhile, the high-speed duct is inactive, with the Mach number at its entrance approximately 1.67. The airflow captured by the high-speed duct alternates between expansion and compression under the influence of the locally expanding mouth and cowl shock, ultimately reaching a Mach number of roughly 1.88 in the isolator.

The variation curve of the exit mass flow coefficient of the high-speed duct (defined as the high-speed duct mass flow divided by the total mass flow captured by both ducts at the initial moment) over time during the mode transition of the inlet operates at  $Ma = 2.0$  was illustrated in Fig. 8. The total time consumed by the splitter from fully open to fully closed and then back to its fully open state is defined as one rotation cycle  $T$  of mode transition, with the abscissa being dimensionless in  $T$ . The splitter's rotation speed in this section is  $\omega = 50^\circ/\text{s}$ , with a period  $T = 0.42\text{s}$ . The graph indicates that the mass flow coefficient entering the high-speed duct gradually increases within the time interval of  $0 < t/T < 0.28$ , remains nearly constant within the interval of  $0.28 < t/T < 0.79$ , and gradually decreases within the interval of  $0.79 < t/T < 1$ .

The time interval of  $0 < t/T < 0.5$  corresponds to a forward transition process. The airflow capture area of the high-speed duct incrementally enlarges as the splitter rotates downwards. However, when  $t/T$

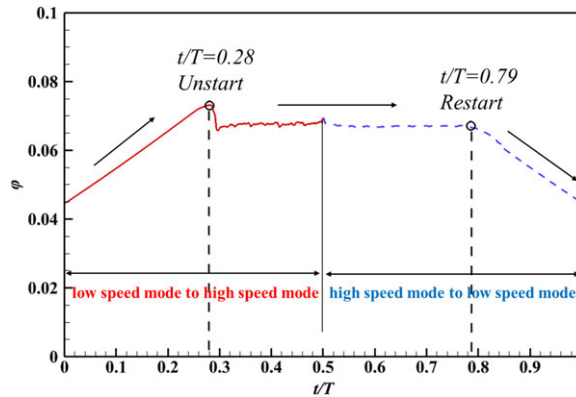


Figure 8. Variation curves of mass flow coefficient of high-speed duct.

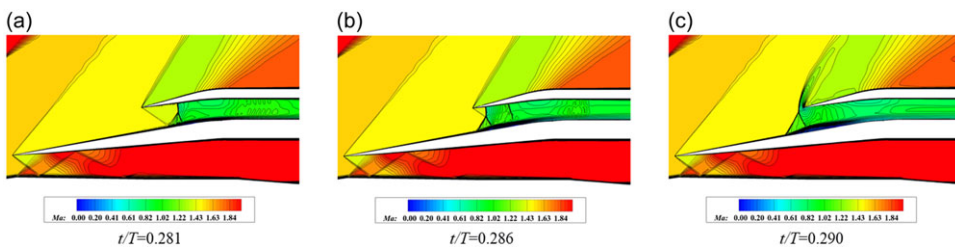
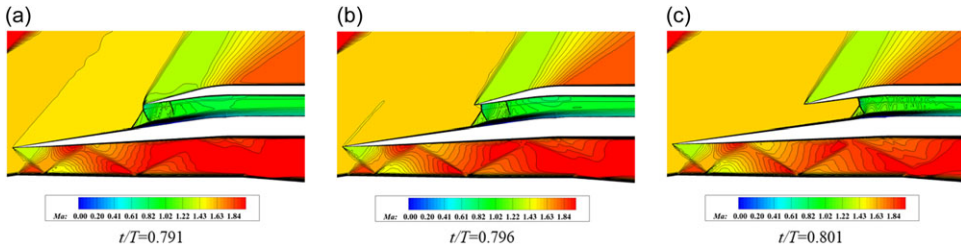


Figure 9. Flow fields near the moment of unstart.

is approximately 0.28 at which the corresponding splitter rotation angle is about  $5.88^\circ$ , the mass flow coefficient abruptly decreases. Given that the capture mass flow should rise with the increase of the duct’s capture area in the starting state, the reason for the mass flow coefficient not increasing but decreasing at  $t/T = 0.28$  can only be attributed to the high-speed duct unstating. Consequently, the moment when the mass flow coefficient shifts from increasing to decreasing during the forward transition process is defined as the time of unstart. The flow field’s evolution near this moment is depicted in Fig. 9. The figure indicates that the terminal shock was rapidly pushed out of the duct, inducing a supersonic overflow at the entrance and causing a sudden decrease in mass flow coefficient. Throughout the subsequent forward transition process, the mass flow coefficient remained virtually unchanged until  $t/T < 0.5$ , signifying that the high-speed duct continued to be in the unstarted state of dynamic mass flow balance maintained by the overflow at the entrance. This suggests that the current aerodynamic configuration struggles to complete the task of mode transition at  $Ma = 2.0$ .

The time interval of  $0.5 < t/T < 1$  corresponds to a reverse transition process during which the splitter gradually opens. However, before  $t/T < 0.79$ , the mass flow coefficient of the high-speed duct did not significantly increase, suggesting that the unstart state of the high-speed duct continued from approximately 0.28 at  $t/T$  to about 0.79 at  $t/T$ . Figure 10 portrays the flow field near this moment, and it’s discernible that the terminal shock gradually recovers into the duct, and the entrance overflow slowly disappears, indicating the duct’s restart. Within the time interval of  $0.79 < t/T < 1$ , the mass flow coefficient progressively decreases until it returns to the value at  $t/T = 0$ . Moreover, by observing Fig. 8, it’s clear that although the geometric conditions (i.e. the splitter’s position) change symmetrically over time during a complete mode transition of the splitter, with  $t/T = 0.5$  as the centre, and the mass flow coefficients at the starting and ending points are almost identical, the evolution process of the mass flow coefficient does not display symmetrical characteristics with  $t/T = 0.5$  as the centre. This implies that at  $Ma = 2.0$  of incoming flow, the high-speed duct not only exhibits a ‘unstart/restart’ phenomenon but



**Figure 10.** Flow fields near the moment of restart.

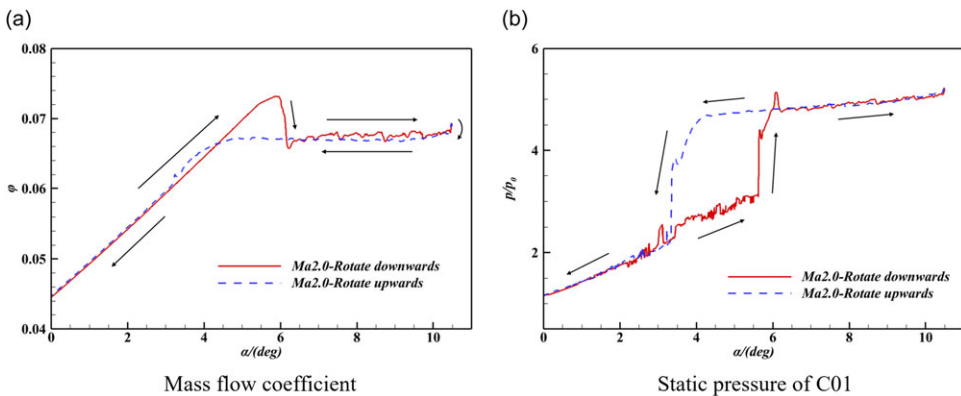


**Figure 11.** Hysteresis loop in unstart/restart process.

also displays hysteresis characteristics. Specifically, if the rotation angle of the splitter deviates from the initial position is ' $\alpha$ ', the high-speed duct of the inlet enters an unstarted state when ' $\alpha$ ' rotates from  $0^\circ$  to approximately  $5.88^\circ$ , yet to restore the starting state, the splitter needs to return to the position of roughly  $4.41^\circ$ .

Figure 11(a) and (b) depict the hysteresis loops for the mass flow coefficient of a high-speed duct and the pressure of C01 on the cowl at  $Ma = 2.0$ . The solid red line symbolises the forward transition process, while the dashed blue line signifies the reverse transition process. These illustrations provide clear insight into the hysteresis characteristics of the 'unstart/restart' occurrence during the mode transition of a high-speed duct. Figure 12 provides a contour map of the Mach number at the significant moments of mode transition. As the splitter rotates downwards, the low-speed duct progressively closes. When the splitter reaches the bottom, its upper surface transforms into the secondary compression surface of the high-speed duct. At this juncture, a large-scale separation bubble emerges on the surface, causing the inlet to unstart. It is noteworthy that the splitter's position at  $t/T = 0.238$  aligns with that at  $t/T = 0.762$ . However, the flow field structure, particularly in the high-speed duct, displays notable variances. Specifically, at  $t/T = 0.238$ , the inlet's high-speed duct is in a starting state. Conversely, at  $t/T = 0.762$ , a separation bubble appears at the high-speed duct entrance, indicating an unstarting state, which is a typical duct flow characteristic.

### 3.2 Scale effect of mode transition

The preceding analysis revealed that when the incoming flow's Mach number is excessively low, there exists a potential for mode transition that can lead to the high-speed duct's failure to start. Once this 'unstart' occurs, the flow characteristics become significantly more complex. As such, under an incoming flow condition of  $Ma = 2.0$ , this section also includes calculations for 0.15, 0.3 and 0.6-fold scaled

**Table 1.** Boundary layer parameters under different scale conditions

Scale	$H_{cap1}$ (mm)	$\delta$ (mm)	$\delta^*$ (mm)	$\theta$ (mm)	$\delta/H_{cap1}$	$\delta^*/H_{cap1}$
0.15	167.4	4.58	1.342	0.355	0.0274	0.0080
0.30	334.8	8.52	2.458	0.646	0.0254	0.0073
0.60	669.6	15.84	4.427	1.169	0.0237	0.0066
1.0	1116	25.22	6.796	1.779	0.0226	0.0061

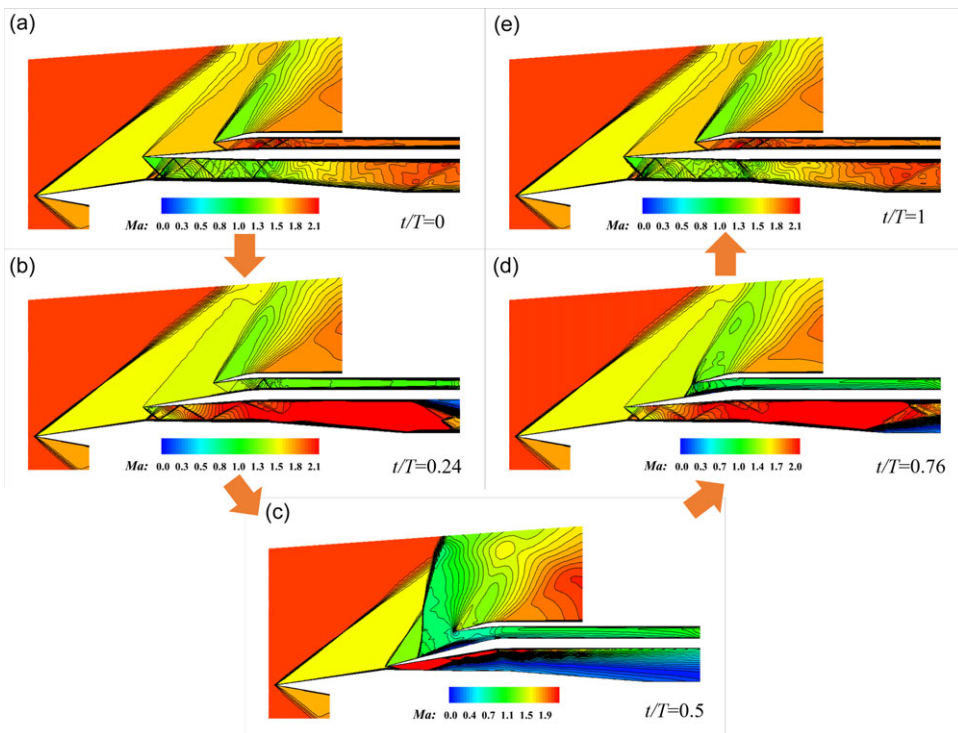


**Figure 12.** Flow fields at significant moments of  $Ma = 2.0$ .

models of the TBCC inlet to scrutinise the scale effect’s influence on mode transition characteristics. For these calculations, the grid distribution near the wall underwent fine-tuning during grid generation so that the near-wall grids of each size model complied with the  $y^+$  near 1 requirement in the first layer. The rest of the grid generation strategy aligns with the prior text. In the ensuing text, *scale* 0.15 denotes a 0.15-fold scaled model, *scale* 0.30 signifies a 0.3-fold scaled model, *scale* 0.60 implies a 0.6-fold scaled model, and *scale* 1.00 corresponds to a full-scale model.

Table 1 catalogues the relevant parameters of the lower wall boundary layer at the entrance of the high-speed duct under varying initial states and scales. Here,  $\delta$  denotes the nominal thickness of the boundary layer,  $\delta^*$  signifies the displacement thickness of the boundary layer, and  $\theta$  represents the momentum thickness of the boundary layer. The data suggests that the larger the model size, the lower the dimensionless values of the nominal and displacement thickness of the entrance boundary layer. This infers that a greater proportion of the main flow passes through the entrance, carrying higher momentum from the upstream flow. As such, larger models can uphold momentum conservation under elevated downstream reverse pressure. Moreover, as the model size increases, the boundary layer evolves further, resulting in a lower incompressible shape factor. Consequently, the duct’s boundary layer in larger models can withstand higher reverse pressure gradients.

**Table 2.** Numerical results under different scale conditions

Scale	$Re(\times 10^6)$	$St(\times 10^{-4})$	$t_{uns}(T)$	$t_{res}(T)$	$\Delta t_{uns}(T)$	$\Delta t_{hys}(T)$
0.15	5.73	9.528	0.284	0.786	0.502	0.07
0.30	11.46	19.056	0.306	0.786	0.48	0.092
0.60	22.92	38.112	0.342	0.786	0.444	0.128
1.0	38.22	63.52	0.372	0.786	0.414	0.158

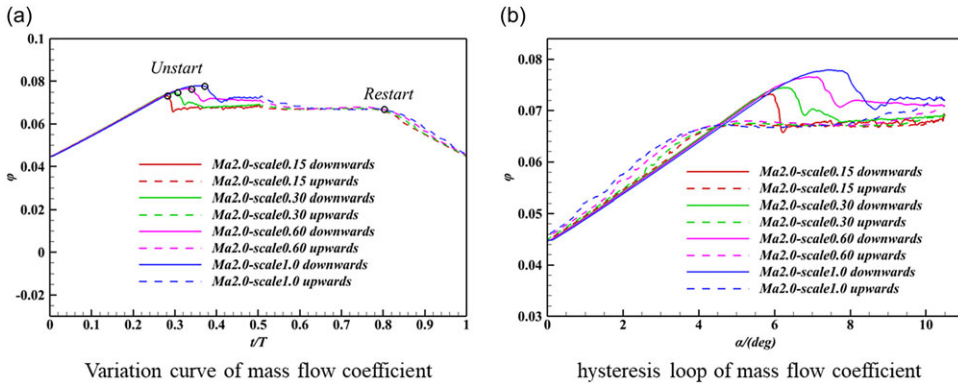


**Figure 13.** Variation curves of mass flow coefficient and relevant hysteresis loop of mass flow coefficient at exit of high-speed duct.

Figure 13(a) illustrates the temporal progression of the mass flow coefficient at the exit of the high-speed duct for different scaled models at  $Ma = 2.0$ . Despite the variance in geometric sizes among the four model sets, the trend in the mass flow coefficient’s variation throughout the mode transition remains qualitatively consistent. Specifically, the captured airflow incrementally increases with the splitter’s downward rotation, abruptly decreases due to the high-speed duct’s unstart, and subsequently settles at a nearly constant plateau value. In the end, the mass flow gradually declines as the high-speed duct restarts. Importantly, larger models enter the unstart state later, but the restart positions among the four sets exhibit minimal differences. Figure 13(b) compares the mass flow coefficient hysteresis loops for different scaled high-speed duct models. The figure reveals that while the scaling effect prompts the inlet’s high-speed duct to enter the unstart state earlier at  $Ma = 2.0$ , the hysteresis degree from unstart to restart is smaller than that in the full-scale model. Thus, despite the larger-sized models later unstart, the flow field is more reliant on historical effects.

Table 2 provides a summary of the  $Re$  number,  $St$  number, unstart time ( $t_{uns}$ ), restart time ( $t_{res}$ ), unstart interval ( $\Delta T_{uns}$ ) and relative hysteresis interval ( $\Delta T_{hys}$ ) of different scale models. The table includes the following calculation formulas:

$$Re = \frac{\rho v d}{\mu} \tag{1}$$

Where  $\rho$  is the incoming flow density,  $v$  is the airflow velocity,  $d$  is the characteristic length (using the splitter length), and  $\mu$  is the viscosity coefficient:

$$St = \frac{f d}{v} \tag{2}$$

Where  $f = \omega/2\pi$ ,  $f$  is the characteristic frequency,  $\omega$  is the splitter’s rotational speed,  $d$  is the characteristic length (using the splitter plate length), and  $v$  is the airflow speed:

$$\Delta t_{uns} = t_{res} - t_{uns} \tag{3}$$

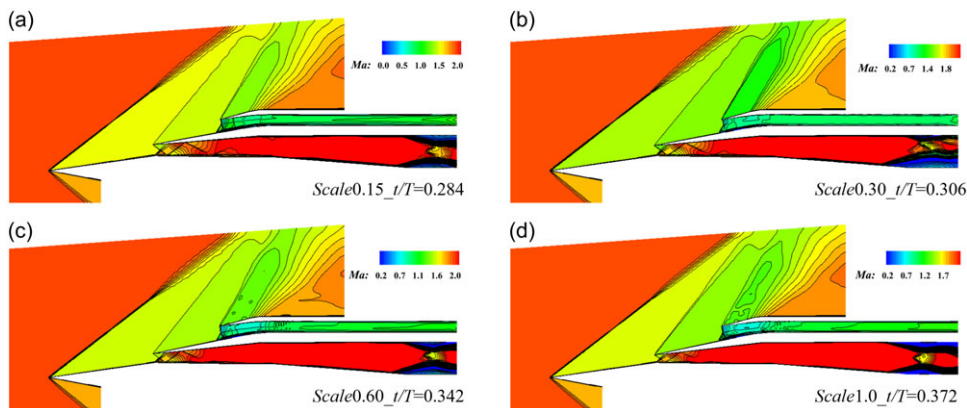


Figure 14. Flow fields at unstart moment under different scale conditions.

$$\Delta t_{hys} = (t_{res} - 0.5T) - (0.5T - t_{uns}) \tag{4}$$

The table indicates that the principal impact of the scale effect is on the unstart time of the high-speed duct. As the scale increases, the unstart time is delayed, however, the restart time doesn't exhibit any significant changes. Hence, the unstart interval decreases and the relative hysteresis interval increases. Figure 14 displays the flow field of different scaled models during the unstart phase, revealing that the flow field remains similar across different scales when the high-speed duct is in the unstart state. The unstart times for the 0.15-fold scaled model, 0.30-fold scaled model, 0.60-fold scaled model and full-size model are  $t_{uns} = 0.284T, 0.306T, 0.342T$  and  $0.372T$ , respectively, and their corresponding splitter angles are  $\alpha = 5.96^\circ, 6.43^\circ, 7.18^\circ$  and  $7.81^\circ$ . In addition, comparisons were made between the unstart interval and the relative hysteresis interval. Based on the full-size model results, the unstart intervals for the 0.15-fold scaled model, 0.30-fold scaled model, and 0.60-fold scaled model were 121.2%, 115.9% and 107.2% of the full-size model, respectively. Meanwhile, the relative hysteresis intervals were 44.3%, 58.2% and 81.0% of the full-size model, respectively.

### 3.3 Analysis of dominant similar criterion number on mode transition

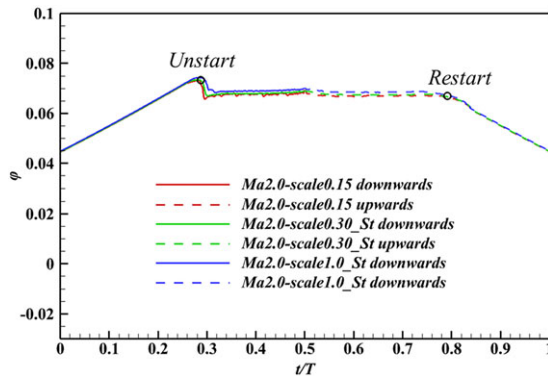
The preceding section dissected and examined how model scaling impacts the mode transition characteristics of TBCC inlet. It was discerned that scaling adjustments also affect two key scale-associated similarity criteria: the  $Re$  number and the  $St$  number. As such, the effects on mode transition characteristics must be a result of a combination of these two criteria. Hence, there is a need to carry out control variable research to pinpoint the dominant similarity criterion.

This section initially explores the influence characteristics of the  $Re$  number alone. Prior studies have maintained a consistent rotational angular velocity  $\omega$  of  $50^\circ/s$ . Therefore, it becomes essential to adjust the rotation speed of the splitter in line with the different scales, ensuring the  $St$  number remains constant. Comparative studies were conducted with the 0.15-fold scaled model, 0.30-fold scaled model and the full-size model. The rotational speeds of the splitter were set at  $50^\circ/s, 25^\circ/s$  and  $7.5^\circ/s$ , respectively. This resulted in corresponding  $St$  numbers of  $9.528 \times 10^{-4}$  and  $Re$  numbers of  $5.73 \times 10^6, 11.46 \times 10^6$  and  $38.22 \times 10^6$ , respectively.

Figure 15 demonstrates that regardless of the model scales, if the  $St$  number is consistent, the mass flow coefficient curves largely coincide. The  $Scale$  1.00 curve is marginally higher than the other two sets of curves due to its highest  $Re$  number and the lowest ratio of the boundary layer thickness at the entrance of the high-speed duct to the duct height. This data not only suggests that the  $St$  number is a vital parameter in controlling the flow characteristics of mode transition, but it also intimates that

**Table 3.** Numerical results under different scale conditions when the  $St$  number is constant

Scale	$Re(\times 10^6)$	$\omega(^{\circ}/s)$	$St(\times 10^{-4})$	$t_{uns}(T)$	$t_{res}(T)$	$\Delta t_{uns}(T)$	$\Delta t_{hys}(T)$
0.15	5.73	50	9.528	0.284	0.786	0.502	0.07
0.30	11.46	25	9.528	0.290	0.786	0.496	0.076
1.0	38.22	7.5	9.528	0.297	0.786	0.489	0.083

**Figure 15.** Variation curves of mass flow coefficient under different scale conditions when the  $St$  number is constant.

the influence of the  $Re$  number is relatively minuscule within the range of  $Re$  numbers studied. The  $Re$  number involved in this study falls within the self-model Reynolds number range. Table 3 offers comprehensive details of the relevant parameters for the three sets of calculation states. It is evident that, contrary to the scaling effect, the degree of change in the unstart moment of the high-speed duct is relatively small, and the unstart interval also undergoes minimal changes. Based on the numerical results of the full-size model, the unstart intervals of the 0.15-fold scaled model and the 0.30-fold scaled model are 102.7% and 101.4% of the full-size model, respectively. The relative hysteresis intervals are 84.3% and 91.6% of the full-size model. The impact magnitude accounts for approximately 10% of the scale effect analysed in the prior section. Figure 16 presents a Mach number contour map of the time when the high-speed duct does not start, with the controlling  $St$  number remaining constant under different  $Re$  numbers. Upon measurement, the splitter angles when the high-speed duct does not start for the 0.15-fold scaled model, 0.30-fold scaled model, and the full-size model were found to be  $5.964^{\circ}$ ,  $6.09^{\circ}$  and  $6.237^{\circ}$ , respectively. These minor changes suggest a negligible impact.

Prior research indicated that the influence range of the  $Re$  number within the self-modeled Reynolds number region accounts for roughly 10% of the scale effect. However, the impact of scaling is noticeably pronounced. It can be deduced that the  $St$  number plays a principal role in the high-speed duct unstart/restart phenomena during the mode transition of TBCC inlet, with an impact range of approximately the remaining 90%. This hypothesis will be validated by establishing two sets of calculation states via the control variable method.

A comparative study was carried out to examine the effects of varying  $St$  numbers on both a 0.3-fold scaled model and a full-size model. For this study, the model scale remained constant, and the  $Re$  number was kept unaltered. The  $St$  number was solely analysed by setting different rotational speeds for the splitter. Figure 17 delineates the temporal evolution of the high-speed duct exit mass flow coefficient under disparate  $St$  numbers, with Fig. 17(a) representing the 0.3-fold scaled model and Fig. 17(b) depicting the full-sized model. From a qualitative standpoint, the  $St$  number does not influence the primary characteristics of the entire mode transition process. However, as the  $St$  number escalates (corresponding to an increase in the splitter's rotation speed), the unstart time is significantly postponed. Table 4 offers

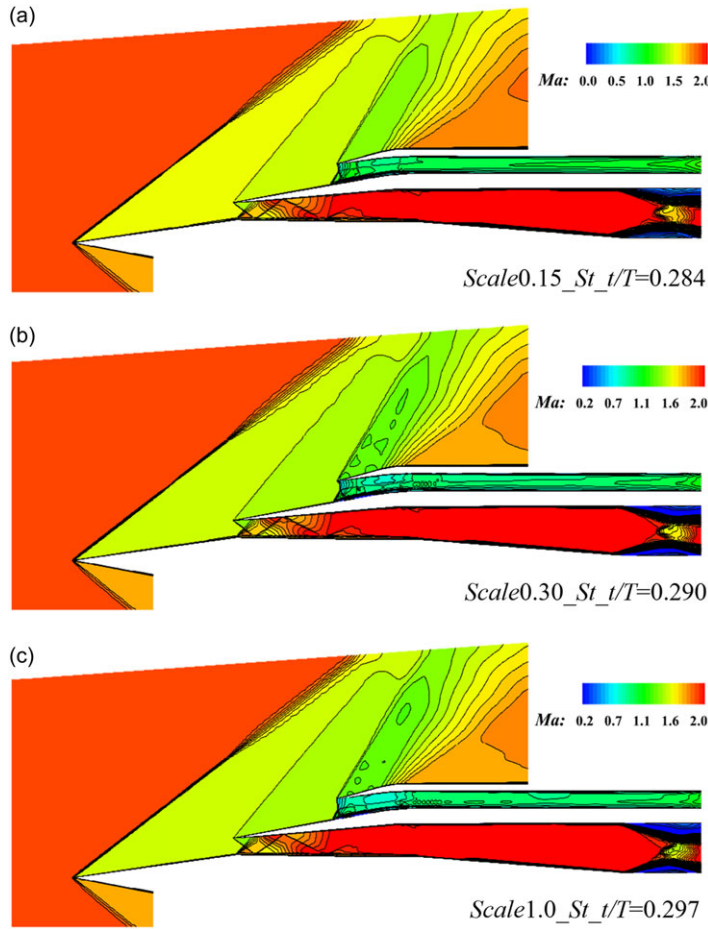


Figure 16. Flow fields at unstart moments under different scale conditions when the  $St$  number is constant.

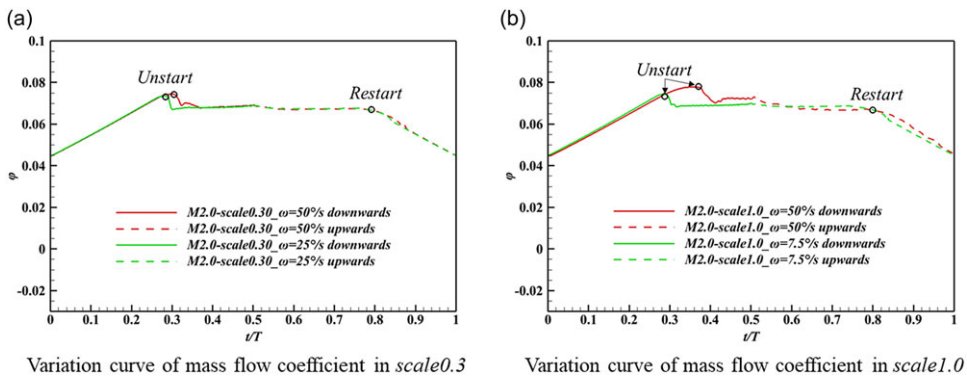
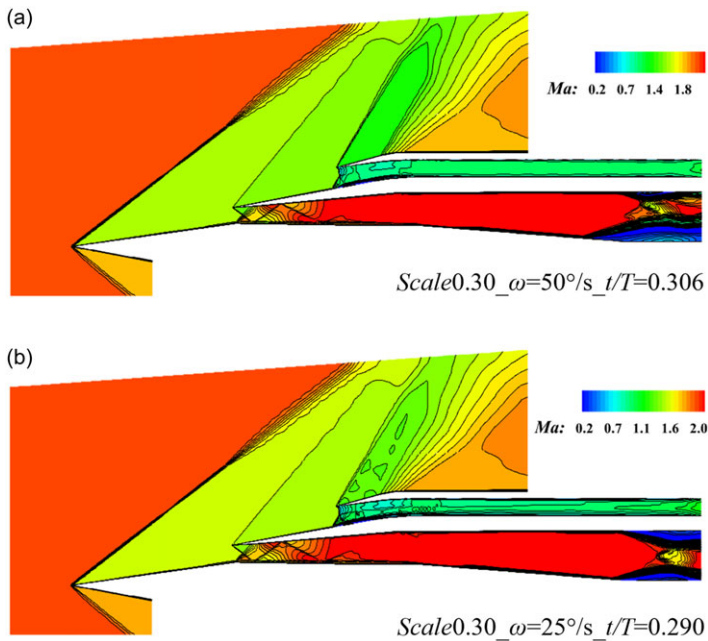


Figure 17. Comparisons of variation curves of mass flow coefficient at different rotation speeds.

**Table 4.** Comparisons of numerical results at different rotation speeds

Scale	$Re(\times 10^6)$	$\omega(^{\circ}/s)$	$St(\times 10^{-4})$	$t_{uns}(T)$	$t_{res}(T)$	$\Delta t_{uns}(T)$	$\Delta t_{hys}(T)$
0.30	11.46	50	19.056	0.306	0.786	0.480	0.092
		25	9.528	0.290	0.786	0.496	0.076
1.0	38.22	50	63.52	0.372	0.786	0.414	0.158
		7.5	9.528	0.297	0.786	0.489	0.083

**Figure 18.** Flow fields at unstart moment under different rotation speeds of scale 0.30.

a comprehensive enumeration of specific calculation parameters and unstart-related instances. For the 0.3-fold scaled model, the  $St$  number ranges from  $19.056 \times 10^{-4}$  to  $9.528 \times 10^{-4}$ , resulting in a 3.23% increase in the unstart interval  $\Delta T_{uns}$  and a 21.05% decrease in the relative hysteresis range. For the full-sized model, the  $St$  number ranges from  $63.52 \times 10^{-4}$  to  $9.528 \times 10^{-4}$ , causing a 15.34% increase in the duration of unstart  $\Delta T_{uns}$  and a 90.36% reduction in the relative hysteresis range. Figures 18 and 19 illustrate the flow fields at two different  $St$  numbers for the 0.3-fold scaled model and the full-size model, respectively, corresponding to the splitter angles of  $6.426^{\circ}$  and  $6.09^{\circ}$ , and  $7.812^{\circ}$  and  $6.237^{\circ}$ , respectively. In conclusion, the data provides sufficient evidence to assert that the  $St$  number significantly influences the unstart characteristics of the high-speed duct during the mode transition process of the TBCC inlet, and exerts a dominant effect relative to the  $Re$  number.

#### 4.0 Conclusions

This study designs a typical over-under TBCC inlet and employs dynamic mesh technology for an unsteady numerical analysis of the inlet's mode transition process. It also investigates the impact of scale alterations on the mode transition process and identifies the dominant similarity criteria. The primary conclusions of the study are as follows:

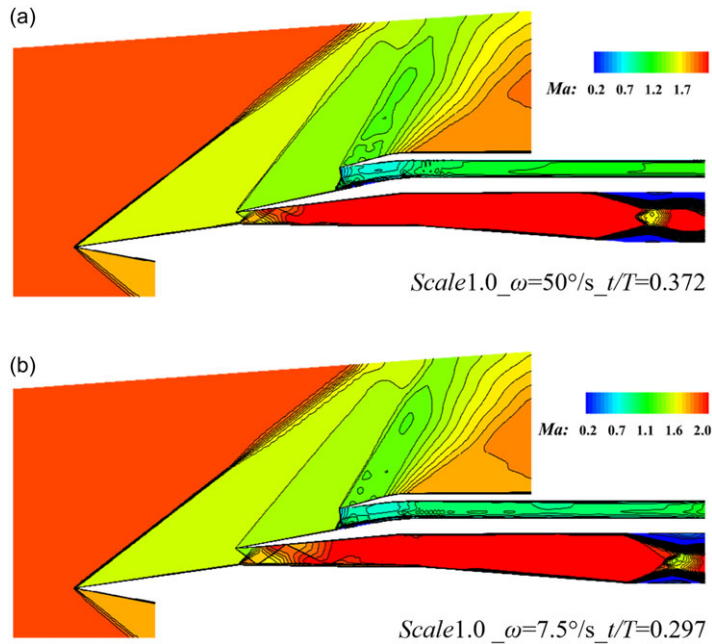


**Figure 19.** Flow fields at unstart moment under different rotation speeds of scale 1.0.

- (1) When the incoming flow resides in an off-design state ( $Ma = 2.0$ ), the high-speed duct manifests an unstarting state during the forward mode transition process, with subsequent flow attributes hinging on historical effects. Throughout the mode transition duration, the flow field parameters display a pronounced hysteresis phenomenon.
- (2) Alterations in scale have a measurable impact on the unstart and hysteresis traits of the inlet. With only the model size being modified, the unstart moment of the high-speed duct is postponed as the model size escalates, while the restart moment remains virtually unaffected. As a result, the entire unstart interval is diminished, and the hysteresis range is larger. At this juncture, the model size adjustment implicates changes in both the Reynolds ( $Re$ ) and Strouhal ( $St$ ) numbers, and the scale effect is attributed to their combined influence.
- (3) When considering the consistency of the  $St$  number and treating the  $Re$  number as a single variable, the unstart characteristics of the inlet are marginally influenced, indicating the  $Re$  number's non-dominant role. However, by maintaining the control  $Re$  number constant and focusing solely on the influence of the  $St$  number under the consistency of scale, it becomes evident that the unstart characteristics of the inlet are significantly impacted, accounting for approximately 90% of the scale effect. This finding confirms that the  $St$  number is the dominant similarity criterion affecting the mode transition process.

**Acknowledgements.** This work was funded by the National Natural Science Foundation of China (Nos. 12172175, 12025202, and U20A2070), National Science and Technology Major Project (J2019-II-0014-0035), Postdoctoral Fellowship Program of CPSF (No. GZB20230970), Science Center for Gas Turbine Project (Nos. P2022-C-II-002-001 and P2022-A-II-002-001), Open Fund from Laboratory of Aerodynamics in Multiple Flow Regimes (No. KLYSYS-KFJJ-ZD-2022-02). The authors appreciate the valuable comments and suggestions of the editorial committee and reviewers.

## References

- [1] Bulman, M.J. and Siebenhaar, A. Combined cycle propulsion: Aerojet innovations for practical hypersonic vehicles, In *17th AIAA International Space Planes and Hypersonic Systems and Technologies Conference*, 2011.

- [2] Hank, J.M., Franke, M.E. and Eklund, D.R. TSTO reusable launch vehicles using airbreathing propulsion, In *42nd AIAA/ASME/SAE/ASEE Joint Propulsion Conference & Exhibit*, 2006.
- [3] Cockrell, C.E., Auslender, A.H., Guy, R.W., et al. Technology roadmap for dual-mode scramjet propulsion to support space-access vision vehicle development, In *AIAA/AAAF 11th International Space Planes and Hypersonic Systems and Technologies Conference*, 2002.
- [4] Stephen, C., Bradford, A.N. and Timothy, R.M. Flight testing the linear aerospike SR-71 experiment (LASRE), NASA Dryden Flight Research Center, 1998.
- [5] Witte, D.W., Huebner, L.D. and Trexler, C.A. Propulsion airframe integration test techniques for hypersonic airbreathing configurations at NASA Langley research center, In *39th AIAA/ASME/SAE/ASEE Joint Propulsion Conference and Exhibit*, 2003.
- [6] Isomura, K., Omif, J. and Murookaf, T. A feasibility study of an ATREX engine at approved Technology levels, In *10th AIAA/NAL-NASDA-ISAS International Space Planes and Hypersonic Systems and Technologies Conference*, 2001.
- [7] Sato, T., Tanatsugut, N. and Hattat, H. Development study of the ATREX engine for TSTO spaceplanem, In *10th AIAA/NAL-NASDA-ISAS International Space Planes and Hypersonic Systems and Technologies Conference*, 2001.
- [8] Sawai, S., Sato, T. and Kobayashi, H. Flight test plan for ATREX engine development, In *12th AIAA International Space Planes and Hypersonic Systems and Technologies*, 2003.
- [9] Hellman, B.M., Bradford, J., Germain, B.S., et al. Two stage to orbit conceptual vehicle designs using the SABRE engine, *Proceedings of AIAA SPACE*, 2016.
- [10] Kuczera, H., Hauck, H., Sacher, P., et al. The German hypersonics technology programme status 1993 and perspectives, In *5th International Aerospace Planes and Hypersonics Technologies Conference*, 1993.
- [11] Sacher, P.W. The engineering design of engine/airframe integration for the SAENGER fully reusable space transportation system, In NATO, 2010.
- [12] Thomas, S.R. TBCC discipline overview. Hypersonics project, In 2011 *Technical Conference*, 2011, No. E-17800.
- [13] Zhang, H.J., Guo, R.W. and Li, B. Research status of TBCC inlet and its key technologies, *Acta Aerodyn. Sin.*, 2010, **28**, (05), pp 613–620 (in Chinese).
- [14] Weir, L., Reddy, D.R. and Rupp, G. Mach 5 inlet CFD and experimental results, In *25th Joint Propulsion Conference*, 1989.
- [15] Albertson, C., Emami, S. and Trexler, C. Mach 4 test results of a dual-flowpath, turbine based combined cycle inlet, In *14th AIAA/AHI Space Planes and Hypersonic Systems and Technologies Conference*, 2006.
- [16] Sanders, B.W. and Weir, L.J. Aerodynamic design of a dual-flow Mach 7 hypersonic inlet system for a turbine-based combined-cycle hypersonic propulsion system, 2008.
- [17] Saunders, J.D., Slater, J.W., Dippold, V., et al. Inlet mode transition screening test for a turbine-based combined-cycle propulsion system, *JANNAF*, (5), 2008.
- [18] Saunders, J.D., Stueber, T.J., Thomas, S.R., et al. Testing of the NASA Hypersonics project combined cycle engine large scale inlet mode transition experiment (CCE LIMX), *58th Joint Army-Navy-NASA-Air Force (JANNAF) Propulsion Meeting*, 2012.
- [19] Foster, L., Saunders, J., Sanders, B., et al., Highlights from a Mach 4 experimental demonstration of inlet mode transition for turbine-based combined cycle hypersonic propulsion, In *48th AIAA/ASME/SAE/ASEE Joint Propulsion Conference & Exhibit*, 2012.
- [20] Clem, M., Woike, M. and Saunders, J., Background-Oriented Schlieren used in a hypersonic inlet test at NASA GRC, In *International Symposium on Flow Visualization*, 2016.
- [21] Yu, H., Zhang, Y., Chen, L., et al. Characteristics of combined-cycle inlet during mode transition in off-design state, *AIAA J*, 2023, **61**, (6), pp 2601–2611.
- [22] Li, N., Chang, J.T., Jiang, C.Z., et al. Unstart/restart hysteresis characteristics analysis of an over–under TBCC inlet caused by backpressure and splitter, *Aerosp. Sci. Technol.*, 2018, **72**, (1), pp 418–425.
- [23] Xiang, X.H., Liu, Y. and Qian, Z.S. Aerodynamic design and numerical simulation of internal over-under Turbine-Based Combined-Cycle (TBCC) inlet mode transition, *Proc. Eng.*, 2015, **99**, pp 129–136.
- [24] Wang, T.C. Aerodynamic experimental techniques, Beijing: National Defense Industry Press, 1986 (in Chinese).
- [25] Jin, Y., Sun, S., Tan, H.J., et al. Flow response hysteresis of throat regulation process of a two-dimensional mixed-compression supersonic inlet, *Chin. J. Aeronaut.*, 2022, **35**, (3), pp 112–127.
- [26] Tan, H.J., Li, L.G., Wen, Y.F., et al. Oscillatory flows of rectangular hypersonic inlet unstart caused by downstream mass-flow choking experimental investigation of the unstart process of a generic hypersonic inlet, *AIAA J.*, 2011, **49**, (2), pp 279–288.
- [27] Van Wie, D.M. Scramjet inlets. In Curran, E.T. and Murthy S.N.B. (eds.), *Scramjet propulsion*. Reston: AIAA, 2001, pp 447–511.